Condensation heat transfer on phase change slippery liquid-infused porous surfaces

Condensation Heat Transfer on Phase Change Slippery Liquid-Infused Porous Surfaces

Raza Gulfam[a], Ting-en Huang [a], Chengxun Lv [a], Daniel Orejon [b,c], Peng Zhang [a,*]

[a] Institute of Refrigeration and Cryogenics, Shanghai Jiao Tong University, No. 800 Dongchuan Road, Shanghai 200240, China

[b] Institute for Multiscale Thermofluids, School of Engineering, The University of Edinburgh, Edinburgh EH9 3FD, Scotland, U.K

[c] International Institute for Carbon-Neutral Energy Research (WPI-I2CNER), Kyushu University, 744 Motooka, Nishi-ku, Fukuoka 819-0395, Japan

*Author to whom correspondence should be addressed: zhangp@sjtu.edu.cn

Abstract

Phase change slippery liquid-infused porous surfaces (PC-SLIPSs) are presented with emphasis on surface wetting characteristics and droplet dynamics influencing the water vapor condensation and the corresponding heat transfer. The functionalized nano-porous copper plate is infused with paraffin wax-xylene solution via dip coating method to prepare PC-SLIPSs., where the droplet dynamics are found to be affected by low adhesion (sliding angle α of 45±5°), high adhesion (α of 60±5°) and slippery (α of 3±1°) states enabled by solid (at 48 °C), mush (at 58 °C) and liquid (at 66 °C) phases. Besides the wettability and droplet adhesion characterization, the condensation heat transfer is particularly explored on PC-SLIPSs under custom-built vacuum-assisted condensation rig. Two major dropwise condensation mechanisms are unveiled depending on the phase of the infused phase change material such as coalescence-induced droplet shedding coupled with droplet sweeping in the solid and mush phases, while discrete-droplet shedding and sweeping in the absence of additional coalescence are reported in the liquid phase. Approximately, 136.8% higher heat transfer coefficients for PC-SLIPS in the liquid phase are reported when compared with the pristine copper surface at low sub-cooling temperatures. In the liquid phase of PC-SLIPSs, theoretical heat flux modeling on dropwise condensation has

been further carried out to elucidate the heat transfer mechanism via a single droplet coupled with the droplet number density. The operational durability of PC-SLIPSs has been found to last for 8±1 hours as confirmed during rigorous condensation experiments. In summary, different wetting features, various droplet shedding mechanisms, promising dropwise condensation modes, high heat transfer coefficient in the liquid phase, and effective time-dependent durability are the salient findings associated with PC-SLIPSs, rendering them competitive alternatives. The most important implication is that the dropwise condensation mode can also underperform if the droplet dynamics is inefficient.

Keywords: SLIPSs, Phase change material, paraffin wax, condensation, heat transfer.

1. Introduction

Dropwise condensation [1-3] is of prime interest to remarkably improve the performance of pristine condensing surfaces in heat transfer applications [4-6]. The hydrophilic nature of the pristine metallic surfaces [7], such as copper tubes and copper plates, prompts filmwise condensation where the condensate develops into a thin film in the order from microns to millimeters [8] imposing an additional thermal resistance with the subsequent suppression of re-nucleation sites. Through bio-inspired surface engineering, attempts have been made to address these drawbacks by tailoring the wetting characteristics of the pristine surfaces, encompassing the creation of micro/nano scaffolds followed by coating with low-surface-energy agents creating the so-called superhydrophobic surfaces (SHSs), which upon further lubricant infusion in the porous matrix results in the widely known lubricant-impregnated/infused surfaces (LISs) [9][10] or slippery liquid-infused porous surfaces (SLIPSs) [11] that have been introduced since 2011 [12]. Although hydrophobic and superhydrophobic surfaces also prompt dropwise condensation mode, it is however drastically threatened because of the fragile layer of the hydrophobic coating and the presence of air-pockets that may both turn into local droplet pinning sites with the suppressed droplet mobility and heat transfer [13]. These challenges have been recently overcome by SLIPSs (or lubricant-infused surfaces) [14] as the lubricant infused can both protect the coating agent as well as avoid the nucleation of droplets in between structures. Nonetheless, the practical application of SLIPSs is currently highly compromised due to lubricant depletion either via cloaking, evaporation or shearing [9][15][16][17]. Therefore, selection of the right condensate-lubricant-surface is the key to the better development and understanding on the fluid SLIPSs intimate interactions for different phases of the lubricant

infused. The slippery materials (the infused lubricants) can be categorized in phase invariant materials (PIMs) and phase change materials (PCMs).

On one hand, PIMs are referred to as lubricants that exist in liquid phase at the ambient temperature such as silicone oils and Krytox GPL oils [12], which upon combination with a porous superhydrophobic surface yield phase invariant SLIPSs (PI-SLIPSs). The understanding of PI-SLIPSs in heat transfer applications has been widely investigated recently. As condensing surfaces, PI-SLIPSs can improve the condensation heat transfer performance by increasing the droplet departure rate and keeping the surface continuously ready for the new condensate [18], which then maintains high nucleation density of the small-sized condensing droplets [19]. PI-SLIPSs can normally maintain the droplet departure rate with droplet sizes in sub-millimeter range, for example, the water droplet with critical radius of 100 μm (or the maximum radius r_{max}) has been reported to be highly mobile during water vapor condensation [14]. In another study, the water droplet with critical radius of 220 μm has been found mobile on hydrophilic PI-SLIPSs, resulting in improved heat transfer coefficients of 113-120% (in presence of 9% non-condensable gases) [20]. In addition to experimental investigations of dropwise condensation, theoretical approaches have emerged especially including PI-SLIPSs through which the droplet population, droplet size distribution, heat transfer through a single droplet, as well as overall heat transfer performance can be predicted and understood. The droplet number density is the key parameter which can be coupled with the heat transfer through a single droplet, predicting the total steady-state heat transfer as originally proposed by Rose [21][22]. It should be noted that the predicted heat transfer via the above method does not account for the thermal conductivity of the surface and the surface wetting characteristics (i.e., contact angles). Later in 2011, Kim and Kim [23] proposed a heat transfer model accounting for the hydrophobic/superhydrophobic

surface underneath the condensing droplets, signifying that the heat transfer via single droplet is affected by successive thermal resistances, in turn being a function of the wetting characteristics with advancing angles of ≥ 90°. Thereafter, Weisensee et al., [24] applied the theoretical model by Kim and Kim on solely nano-structured SLIPSs in order to elucidate the heat transfer through individual condensing droplets accounting for the additional heat transfer resistances imposed by the solid surface and the lubricant oil presented in between the structures. Further, theoretical droplet heat transfer was then coupled with experimental observations where the critical droplet radius (r_{max}), nucleation radius (r_{min}), and droplet number density to estimate the different steady state heat transfer performance function of the solid fraction and height of the nano-structures amongst others. This approach demonstrates that the droplet size distribution is a pivotal parameter required to accurately predict the heat transfer on hydrophobic, superhydrophobic, SLIPSs and/or other surfaces where dropwise condensation ensues. Recently, Maeda et al., [25] theoretically modeled various PI-SLIPSs based on the droplet number density and single-droplet heat transfer approach taking into account the thermo-physical properties and the size of the surface structures as well as the lubricant thickness presented below the condensing droplets. Despites the greater nucleation densities reported on micro-/nano-structured PI-SLIPS when compared to solely nano-structured ones, their results showed a 100% better heat transfer for nano-structured PI-SLIPSs when compared to hierarchical micro-/nano-structured ones as the presence of micro-structures and the layer of oil in between introduces an additionally thermal resistance. Also, Ho et al., [26] theoretically modeled the heat transfer through liquid-infused surfaces for low-surface tension fluids undergoing phase-change in a dropwise condensation manner, establishing a good fit for the droplet number densities and the maximum droplet radii. In another study by Sirohia and Dai [13], liquid-infused slippery rough surfaces have been

subjected to condensation heat transfer, and a theoretical model considering the thermal resistances predicted the heat transfer as the function of contact angles and contact angle hysteresis. It was concluded that high contact angle hysteresis led to low heat transfer coefficients as a consequence of the larger critical droplet radii ensuing. Based on these predictions (the case with constant contact angle), the reduction in heat transfer coefficients has been demonstrated at large critical droplet radii.

On the other hand, PCMs are defined as the materials that can reversibly change physical phases from solid to liquid and liquid to solid at the melting and freezing temperatures, respectively [27]. PCMs can be categorized in waxy (e.g., paraffin waxes) and non-waxy (e.g., fatty acids), depending on the characteristics such as the length of the carbon chain, the presence or absence of double bond between carbon molecules and the functional group termination, which in turn induces different oiliness, thermo-responsiveness and fluidic features [28]. By infusing waxy PCMs into micro/nano-porous substrates, phase change SLIPSs (PC-SLIPSs) where the wetting functionalities can be tailored in different phases encompassing solid, mush and liquid, depending on the imposed operational temperature [29]. When PC-SLIPSs are prepared, each phase imposes a unique wettability and wetting mode inducing the different droplet dynamics. PC-SLIPSs made of paraffin waxes can withstand high operational temperatures, and they have been recently applied to droplet manipulation [30][31][32], optical transparency control [33], oil/water separation [34], anti-icing [35][36], photo-thermally responsive-deicing [37] and condensation phase-change [29][38]. PCMs are found to be superior over the conventional slippery liquids in several aspects. The waxy PCMs such as paraffin waxes can efficiently prohibit the cloaking, while conventional liquids (Krytox oils, and silicon oils, etc) induce the cloaking. At the ambient temperature, the evaporation of

conventional liquids cannot be avoided in open space, resulting in self-deterioration of SLIPSs; while the employed paraffin wax is converted into the solid phase where no evaporation can occur and self-deterioration can be avoided. At high temperatures, the evaporation of already-existing conventional liquids can be much increased compared with the PCMs that tend to just start evaporating above their melting temperature. PCMs such as paraffin waxes are environmental-friendly and immiscible with water, i.e., if water harvesting is done via condensation on PC-SLIPSs, the collected water does not deem to be polluted, and PCMs can be separated by adopting physical separation techniques. In contrast, the miscibility of conventional liquids with water is widely known, polluting the water that would need post-separation by adopting the cost-intensive chemical separation techniques.

In this paper, paraffin wax-xylene solution has been infused into nano-porous oxidized copper plate by dip-coating method, leading to PC-SLIPSs. The objective is to study the surface wetting features and then subject the PC-SLIPSs to condensation of water vapors in the solid, mush and liquid phases of PC-SLIPSs, emphasizing the droplet dynamics, the condensation mechanisms and the corresponding heat transfer. Experimental observations of nucleation, growth, coalescence and shedding, i.e., droplet number density, are then coupled with the proposed thermal resistance based theoretical model through single droplet to elucidate the role of droplet dynamics and droplet radii. Two condensation mechanisms named as coalesced-droplet shedding-sweeping and discrete-droplet shedding-sweeping, driven by the different phases of PC-SLIPSs have been unveiled. The liquid phase of the PC-SLIPSs provides higher experimental and theoretical heat transfer coefficients achieved via direct dropwise condensation, empowering enhanced discrete droplet shedding and sweeping mechanism than that of the mush and solid phases also performing in dropwise condensation and that of pristine

copper plates performing in filmwise condensation. We conclude on the different droplet shedding dynamics and condensation heat transfer performance function of the phase of the lubricant infused, i.e., temperature of operation, for the very same surface.

2. Experimental methods

2.1. Fabrication of PC-SLIPSs and surface characterizations

PC-SLIPSs are fabricated by infusing the paraffin wax-xylene solution into the nano-porous scaffold (oxidized layer) of superhydrophobic copper plate [39]. The complete fabrication procedure from the pristine copper plates to the PC-SLIPSs is schematized stepwise in Fig. 1.

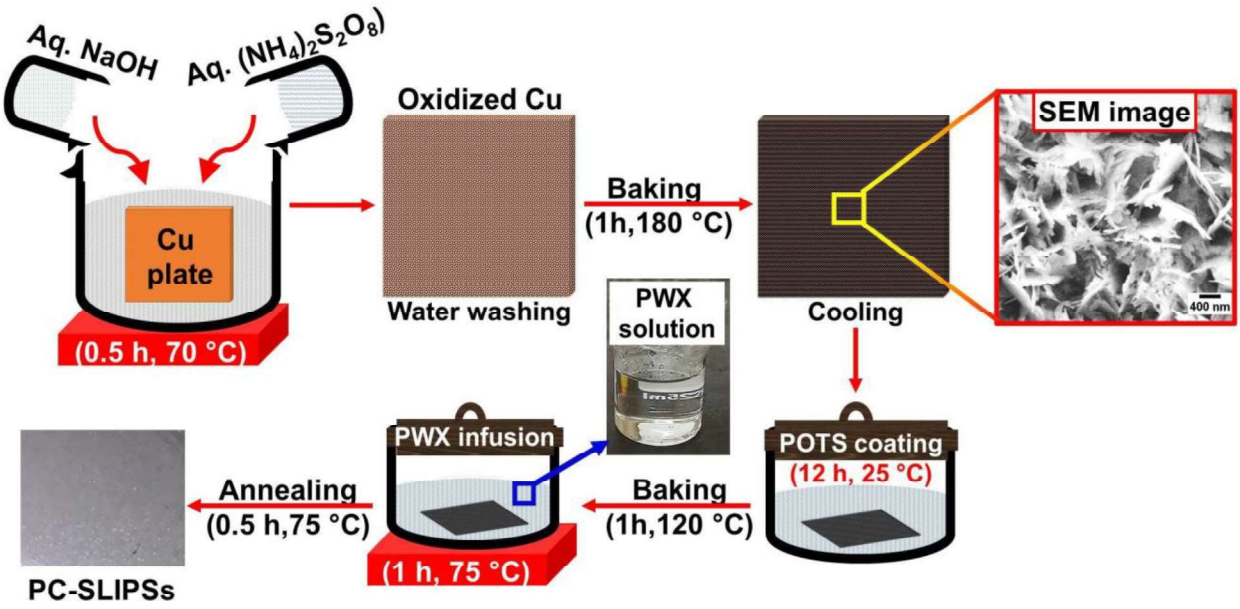

Fig. 1. Fabrication process of the PC-SLIPSs from oxide nano-structure growth on pristine copper plate and functionalization to paraffin wax-xylene (PWX) infusion and annealing. SEM image shows the randomly-dispersed nano-sheets/blades (Scale bar is 400 nm).

A copper plate with dimensions of 20mm×20mm×0.4mm has been used as the substrate which is successively washed with acetone, ethanol and distilled water. Afterwards, 2.5 M aqueous solution of sodium hydroxide (NaOH) and 0.1 M aqueous solution of ammonium persulfate [$(NH_4)_2S_2O_8$] are prepared separately via hand stirring. After obtaining the clear

solutions, they are both mixed to produce an alkaline solution (pH of 14) in which the pristine copper plate is dipped followed by heating at 70 °C for 0.5 h, leading to the oxidized copper plate with blade like nano-structures, as shown in Fig. 1. After washing with excess of distilled water, the oxidized copper plate is baked at high temperature of 180 °C for 1 h, which is thereafter cooled to ambient temperature and then functionalized by dipping in a solution of 1 wt.% POTS-in-ethanol (perfluorooctyltriethoxysilane) for 12 h at the ambient temperature. Subsequently, the functionalized copper plate is baked at 120 °C for 1 h. Next, PC-SLIPSs are prepared by dipping (different method compared with our previous work of spin coating [29]) the functionalized copper plate in the paraffin wax-alone or paraffin wax-xylene (PWX) solution (as depicted in Fig. 1) at temperature of 75 °C for 1 h. Regardless of the stoichiometric quantities for PWX solution, enough quantity of xylene is used to fully mix with the paraffin wax (15 mL xylene and 3 g paraffin wax in this study). However, it should be noted that xylene cannot mix with the paraffin wax at the ambient temperature as it is in the solid phase. Therefore, temperature (75 °C) higher than melting temperature of paraffin wax (60-62 °C) has been maintained throughout the coating process. Thermal annealing (see the scheme of thermal annealing in Fig. S1a Supplementary Material) has been implemented on the PC-SLIPSs as the final fabrication step. It should be noted that the paraffin wax-alone could not help stop the liquid drainage during thermal annealing (see Fig. S1b in Supplementary Material), meaning that the infusion of paraffin wax is not sufficient. Whilst, the liquid drainage has not been observed in the case of PWX-infused PC-SLIPSs (see Fig. S1c in Supplementary Material).

Wetting characteristics of all surfaces (pristine copper plate, oxidized copper plate, superhydrophobic copper plate and PC-SLIPSs) have been determined by optical goniometer (OCA 20). The surface morphology of oxidized copper plate has been analyzed by SEM

(ZEISS), while those of PC-SLIPSs in solid and mush phases have been examined at high temperatures (48 °C and 58 °C) by erecting a setup of Peltier device-digital light microscope. The average roughness of thermally-annealed PC-SLIPSs in solid phase (ambient temperature ~25 °C) have been determined by confocal laser scanning microscope (WT2LSMZ01).

2.2. Experimental setup for condensation heat transfer

The vacuum-assisted condensation rig has been designed and fabricated, as shown in Fig. 2. The rig is composed of the cylindrical environmental chamber of DN200×100mm with a glass chamber window (DN200×20mm). A copper-block welded with a chiller (heat exchanger providing the water input and output) opens into the condensation chamber. An electric steam generator of 440mm×330mm×600mm with water capacity of 5 L is employed to create steam with the help of a coil heater of variable power between 0-3000 W. A super-heater of 3000 W has also been employed along the steam line to maintain the steam quality. Other auxiliaries include the condensate drum of 5 L, a steam flow controller, a vacuum pump, a pressure transducer, a thermostatic bath, four thermocouples, a digital camera (Point Grey) and a data acquisition system (Agilent, 34972A).

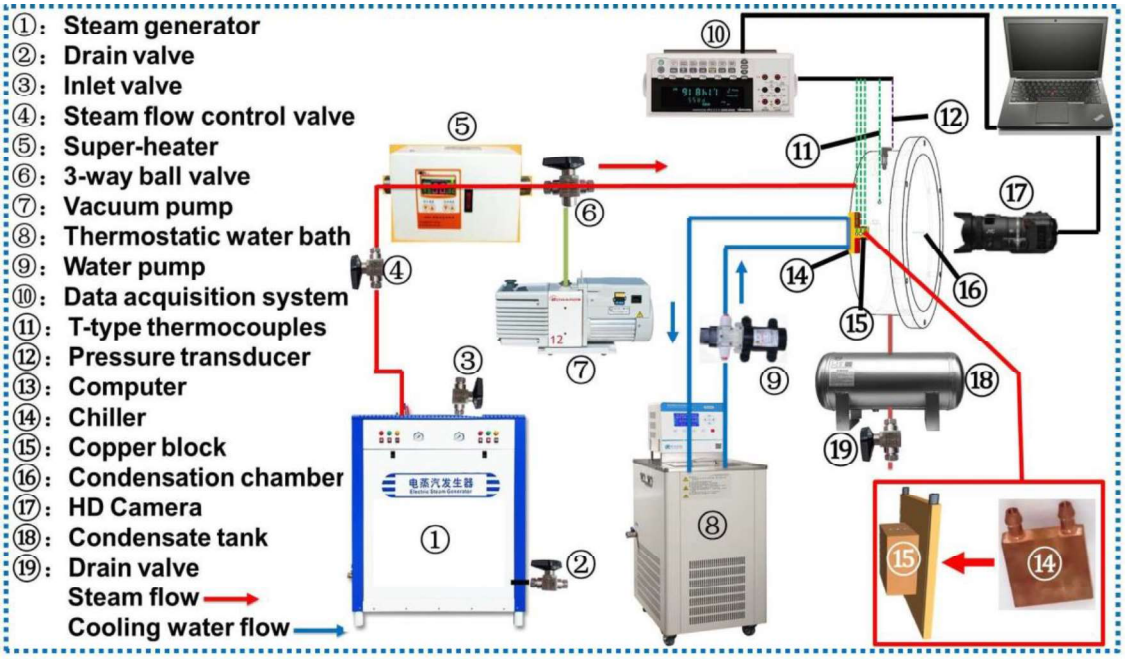

Fig. 2. Custom-built experimental setup for the vacuum-assisted condensation heat transfer analysis and measurements. The different equipment and elements of the setup are numbered and included in a legend within the figure. Bottom-right shows magnified views of the chiller (14) and copper block (15) used in the setup.

The environmental chamber is well-insulated by using polymeric foam to avoid heat losses. Prior to running the experiment, water is vigorously boiled to remove any presence of non-condensable gases within the condensing fluid. Subsequently, in order to further remove the presence of non-condensable gases from the environmental chamber and from inside the pipes, the environment is evacuated by running the vacuum pump for 2 hours, and then the system is purged by the steam from the steam generator. Vacuuming and purging are repeated several times. The chiller temperature T_c (°C) is maintained through the water supply from a thermostatic bath (DC-2020, CNSHP) by means of centrifugal pump (PLD-1205). By varying the temperature of thermostatic bath, the chiller temperature T_c (°C) can be changed to maintain the surface temperature T_{surf} (°C), thereby obtaining the desired sub-cooling temperatures T_{sub} (°C) defined as T_s–T_{surf}. The steam enters the condensation chamber from the separate steam

generator with the steam temperature T_s (°C) controlled by changing the voltage of the steam generator. The steam pressure is measured through a pressure transducer vertically mounted on the condensation chamber, while the steam temperature is measured near the condensing surface by a suspended thermocouple. The steam temperature T_s (°C) and the local temperatures along the copper block T_1, T_2 and T_3 (°C), with T_3 the closest to the condensing surface, are measured via T-type thermocouples (Ø0.5mm), as shown in Fig. S2 in Supplementary Material. Before the data acquisition, the prototype is operated long enough such that the steady state condensation heat transfer conditions are reached, and eventually, the steam pressure, steam temperature and local temperatures alongside the copper block are recorded via computer-based data acquisition system with 1 s data storage interval. The custom-built condensation unit has been experimentally and theoretically validated, as shown in Fig. S3 in Supplementary Material. For the condensation on PC-SLIPSs, the experiments have been conducted at varying steam temperatures between 45-70 °C and the corresponding steam pressures of 9.5-31.2 kPa. The surface temperatures on PC-SLIPSs in solid, mush and liquid phases have been maintained by regulating the temperature of chiller via thermostatic bath. During the experiments, videos have been recorded through digital camera (Point Grey) at 30 fps. The condensed vapor on the glass window of the condensation chamber usually impedes the clear capture of the condensation phenomenon, which was controlled by blowing hot air during the video capturing process.

3. Results and discussion

3.1. Wetting and morphological characteristics of PC-SLIPSs

The wetting characteristics of PC-SLIPSs have been analyzed by measuring the apparent contact angles, sliding angle α (°), as well as the advancing θ_{adv} (°) and receding θ_{rec} (°) angles in

solid, mush and liquid phases via water droplet of about 5 μL, as presented in Table 1. Before thermal annealing, no droplet sliding ensues even at titling angles as high as 90° for PC-SLIPSs in the solid phase as a consequence of the strong adhesion and contact line pinning. After thermal annealing, the low adhesion and slippery states are achieved in the solid phase and liquid phase, inducing the droplet mobility with sliding angles of 45±5° and 3±1°, respectively. The slippery nature of PC-SLIPSs in the liquid phase is in agreement with the literature where α is less than 5° [40][41]. The mush phase (between solid and liquid phases) provides the high adhesion with sliding angles of 60±5°. The greater adhesion in the mush phase is due to the co-existence of the solid and liquid phases introducing additional pinning sites. Further evidences on low adhesion state in solid phase and high adhesion state in mush phase can be seen from the surface morphologies as presented next.

Table 1. Wetting characteristics of PC-SLIPSs. Standard deviation has been calculated from three independent measurements.

Phases/Angles	Surface temperature (°C)	Sliding angle α (°)	Apparent CA	Advancing angle θ_{adv} (°)	Receding angle θ_{rec} (°)
Solid phase	48	 45±5°	112±1°	113±1°	107±1°
Mush phase	58	 60±5°	116±1°	118±2°	106±2°
Liquid phase	66	 3±1°	108±1°	107±1°	106±1°

The surface morphology and average surface roughness R_a of PC-SLIPSs in solid phase have been determined at ambient temperature by employing the confocal laser scanning microscopy (inspected area of 250μm×250μm), as depicted in Fig. 3a. PC-SLIPSs consist of randomly

dispersed heterogeneities (clearer in the corresponding colored image of Fig. 3a), which are accountable for R_a of 0.80±0.06 µm in the solid phase at ambient temperature. Surface roughness of the PC-SLIPSs in solid and mush phases at high temperatures could not be measured because of the operational limitation of the confocal laser microscopy. Therefore, a setup has been erected by mounting the PC-SLIPSs on the Peltier device, which was then set under the digital microscope. By controlling the electric voltages of the Peltier device, the temperature of PC-SLIPSs has been maintained at 48 °C and 58 °C to observe the solid and mush phases, respectively.

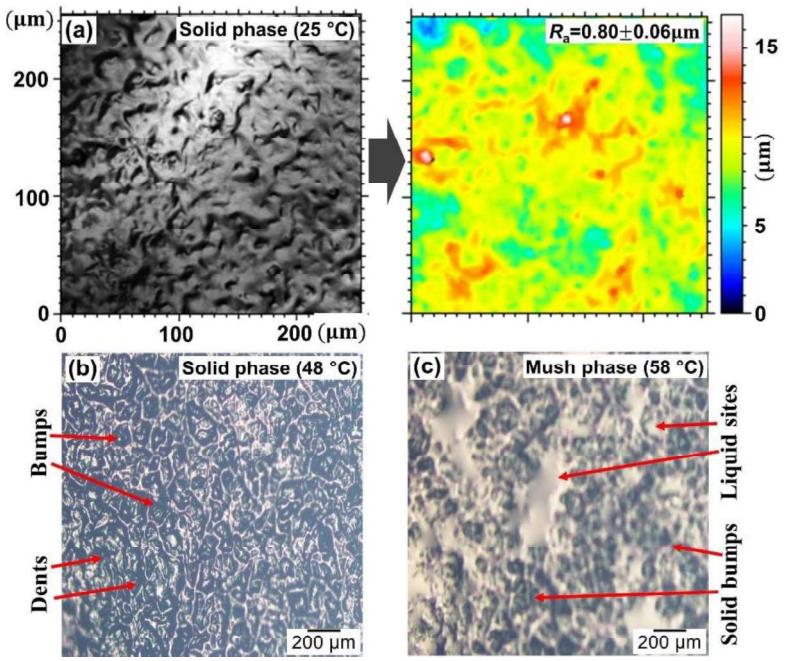

Fig. 3. Surface morphology of PC-SLIPSs in (a) solid phase at ambient temperature of 25 °C and the corresponding color demonstrating the surface roughness, (b) solid phase at 48 °C demonstrating bumps and dents, and (c) mush phase at 58 °C depicting liquid sites and solid bumps

The surface heterogeneities consisting of bumps and dents (Fig. 3b) have been observed at 48 °C in solid phase (similar to those of the solid phase at 25 °C), inducing the low adhesion state as discussed above. While at 58 °C, liquid sites and solid bumps appear (Fig. 3c), demonstrating the

co-existence of solid-liquid phases which is known as the mush phase. Indeed, paraffin wax is itself a mixture of several petroleum waxes that have various melting points, i.e., near the melting temperature, some would start melting sooner, referring to the liquid sites; and some would melt later, referring to the solid bumps. Paraffin wax is also amorphous in nature, consisting of randomly distributed waxes when observed on the surface, i.e., solid bumps and liquid sites are not regularly arranged. All these factors are expected to stimulate the imbalance of droplet contact line in the mush phase, resulting in relatively high adhesion state that drastically affect the droplet dynamics as encountered while measuring the sliding angles.

3.2. Droplet dynamics, condensation heat transfer coefficients and durability analysis

The condensation patterns on the pristine copper plate and PC-SLIPSs are depicted in Fig. 4. On one hand, as a consequence of the hydrophilic characteristics of the pristine copper plate, the expected filmwise condensation behavior ensues as demonstrated in Fig. 4 (a-d). The condensate initially nucleates and grows with droplets in the wetting regime, i.e., contact angles below 90°. Droplets are highly pinned on the surface and grow via direct condensation and coalescence until they form a macroscopic film all over the surface. On the other hand, on PC-SLIPSs condensation ensues in a dropwise fashion as demonstrated in Fig. 4 (e-p). For PC-SLIPSs in the solid phase at surface temperature T_{surf} = 48 °C (Fig. 4 (e-h)), dropwise condensation patterns are ascribed to the inherent hydrophobicity and topography of the wax infused in the PC-SLIPSs, enabling the low adhesion state. During dropwise condensation on PC-SLIPSs, droplet shedding is favored by gravitational forces pulling the droplet downwards while pinning forces oppose to the motion. In this case, the biggest droplets are formed via coalescence-inducing droplet shedding from the surface for droplet sizes in the order of a millimeter. Here the droplet shedding/departure mechanism adopted is that of coalescence-induced shedding where the

droplet gains enough mass so that gravitational force overcomes that of pinning. However, the droplet departure is not efficient enough as droplets are as big as 500 μm in radius with shedding time t_s as large as 15-16 s, as presented in Fig. 4 (e-h). The t_s here is defined as the interval counting the onset of droplet growth until it starts moving and shedding on the surface. When looking into the condensation patterns in the mush phase (Fig. 4 (i-l)) at surface temperature T_{surf} ≈ 58 °C, dropwise condensation ensues and droplets typically shed following a coalescence event seemingly to the behavior observed in the solid phase. However, the droplet shedding time t_s is almost two-fold higher (30-31 s) with droplet sizes as large as 700 μm in radius (Fig. 4 (i-l)). The longer shedding times and the larger sizes of the shedding droplets are a direct evidence of the higher adhesion state incurred by the mush phase. The heterogeneous nature of the mush phase where solid and liquid phases co-exist is responsible for the strong pinning of the contact line that directly affects droplet mobility [29].

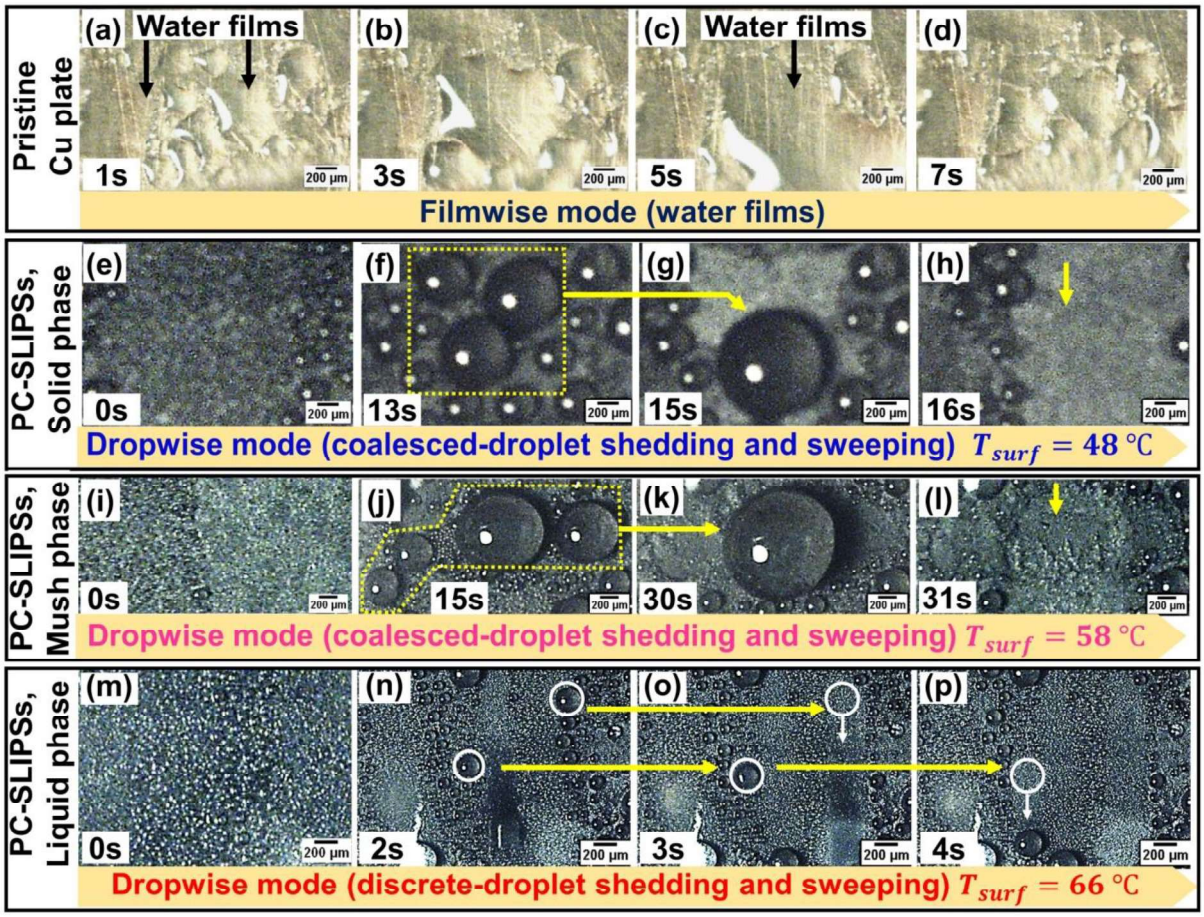

Fig. 4. Transient condensation patterns on (a-d) pristine copper plate, (e-h) solid phase, (i-l) mush phase, and (m-p) liquid phase of PC-SLIPSs at T_{sub} of 0.7°C. Scale bars are 200 μm. The contrast of the images has been enhanced to make the droplets more evident. Vertical arrows pointing down additionally represent the direction of gravity. Snapshots presented illustrate the growth, coalescence and shedding event where t = 0 second as the time right after a shedding event takes place (except in the case pristine copper). Surfaces are placed in the vertical direction and gravity pulls the droplets from top to bottom. The images provided here are cropped from the actual images captured during the condensation, and the shedding time shown here is based on the single experiment to depict the departure at the right moments.

In the liquid phase (Fig. 4 (m-p)) at surface temperature T_{surf} = 66 °C (above the PCM melting temperature), the condensation also ensues in a dropwise fashion as for the solid and mush phases; nonetheless, the shedding mechanism uniquely consists of either discrete droplet mobility or the sweeping of small-sized droplets without the need for a major coalescence event to occur. The size of the shedding droplets on PC-SLIPSs in the liquid phase and the droplet

departure times are remarkably decreased when compared to the solid and mush phases, with droplet sizes below 300 μm in radius and shedding times as quick as t_s of 3-4 s for this particular slippery state. The different droplet sliding behavior presented should in turn condition the heat transfer coefficient h in each phase. As expected, it can be concluded that the largest the sliding angle, the lowest is the shedding performance (mush phase); whereas the smallest the sliding angle, the largest is the shedding and the expected heat transfer performance during condensation (liquid phase).

Next, we characterize the different droplet evolution in each phase of the PC-SLIPSs, by differentiating between droplet growth and droplet shedding regimes defined by the droplet growth radius r_{gd} (μm) and critical droplet radius r_{cd} (μm), respectively, which are presented in Table 2. The r_{gd} (μm) is defined as the droplet radius in the growing regime via both direct condensation and coalescence before reaching r_{cd} (μm). The r_{cd} (μm) is defined as the necessary radius for the shedding of the droplets to initiate from the surface.

Table 2. Droplet size ranges (μm) and shedding times (s) evolution regimes in solid, mush and liquid phases of the PC-SLIPSs. Standard deviation has been estimated based on five cycles in three independent experiments.

Phases	**Growing regime r_{gd} (μm)**	**Shedding regime r_{cd} (μm)**	**Shedding time (s)**
Solid	< 500	500-530	15±2
Mush	< 650	650-760	29±3
Liquid	< 220	220-300	4±1

In the solid phase, the growing regime defined as droplet growth mainly via direct condensation and coalescence with neighboring droplets ensues until droplets reach the critical droplet radius for the shedding regime radius, i.e., r_{cd} > 500 μm, at which droplets start shedding

from the surface. Droplet motion in the shedding regime for droplets with radius of 500 μm is triggered via both gravity and coalescence with neighboring droplets evidencing the relatively low adhesion of the PC-SLIPSs in the solid phase. In the mush phase, the droplets with radii below 650 μm are found in the growing regime. After coalescing, they enter the shedding regime with r_{cd} in the range of 650-760 μm. With increasing departure radii of the droplets, the heat transfer performance is drastically affected [4], which is anticipated to be lower in solid phase and mush phase when compared to the liquid phase of the PC-SLIPSs. Droplets growing on both solid and mush phases need for the occurrence of a coalescence event for the contact line to depin from the surface and for the droplet to enter the coalescence-induced droplet shedding regime. In the liquid phase, the growing regime contains the droplets with radii below 220 μm that grow also via both direct condensation and coalescence until they enter the discrete-droplet shedding and sweeping regime with r_{cd} in the range of 220-300 μm. The departure or shedding radius is comparable to the critical departure radius reported on hydrophilic SLIPSs by Guo and Tang [20]. Therefore, the smaller shedding sizes r_{cd} in the liquid phase when compared to solid and mush phases are empowered by the liquid slippery state of the infused lubricant in the PC-SLIPSs. In summary, the overall condensation mode reported on PC-SLIPSs for all phases is that of dropwise; however, the different phases induce different wettability and surface topographies that can be tailored to further control the main shedding mechanism and the critical droplet radius.

Next, we present a preliminary comparative heat transfer analysis where the heat transfer coefficient h ($kWm^{-2}K^{-1}$) versus T_{surf} (°C) for pristine copper plate as well as for the PC-SLIPSs in solid, mush and liquid phases is presented in Fig. 5. The solid phase, mush phase and liquid phase are achieved by the different surface temperatures T_{surf} of 48 °C, 58 °C and 66 °C,

respectively. Owing to the existence of mush phase in a relatively constrained temperature range between 53-59 °C and with continuous shift between the liquid and solid phases, it is rather difficult to maintain different steady state conditions such as the sub-cooling temperature during condensation experiments in the mush phase. Therefore, the comparative data is solely presented at a single T_{sub} = 1.5 °C.

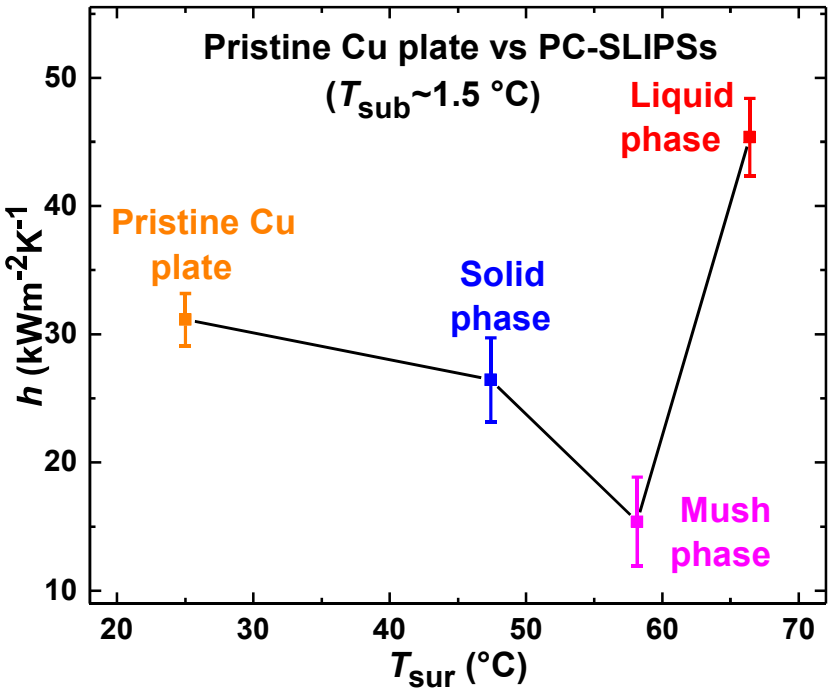

Fig. 5. Heat transfer coefficient h (kWm^{-2}K^{-1}) versus surface temperature T_{sur} (°C) at fixed sub-cooling temperature T_{sub} = 1.5 °C on the pristine copper plate and on PC-SLIPSs in the solid, mush and liquid phases.

The h on pristine copper plate, solid phase, much phase and liquid phase are 31.1 kWm^{-2}K^{-1}, 26.5 kWm^{-2}K^{-1}, 15.4 kWm^{-2}K^{-1} and 45.6 kWm^{-2}K^{-1}, respectively, indicating that the PC-SLIPSs behave quite differently depending on the imposed phase controlled by the working temperature of the cooling fluid. A 46.6% increase in the heat transfer coefficient h is reported on PC-SLIPSs in the liquid phase when compared to the pristine copper, while a 14.8% decrease and a 50.5% decrease on the heat transfer coefficient h is reported for the PC-SLIPSs in solid and mush

phases when compared to the pristine copper, respectively. When looking into different heat transfer coefficients of the PC-SLIPSs, it can be seen that h varies greatly depending on the phase. In the solid and mush phases, rather low h when compared to the pristine copper is ascribed to the large r_{cd}, i.e., long time span of the growing regime before shedding taking place for both phases. Conversely, the liquid phase provides the effective shedding of small-sized droplets with high shedding frequency, providing h ($kWm^{-2}K^{-1}$) higher than that on the pristine copper plate, solid phase and mush phases. Based on the above characterization and discussion, the liquid phase of the PC-SLIPSs is the most attractive and it is of the outermost fundamental interest, because it can ensure the efficient droplet departure of small-sized droplets. Therefore, herein we focus on further investigating the liquid phase to establish the heat flux q and heat transfer coefficient h dependence on T_{sub}. The results are shown in Fig. 6a and Fig. 6b, respectively.

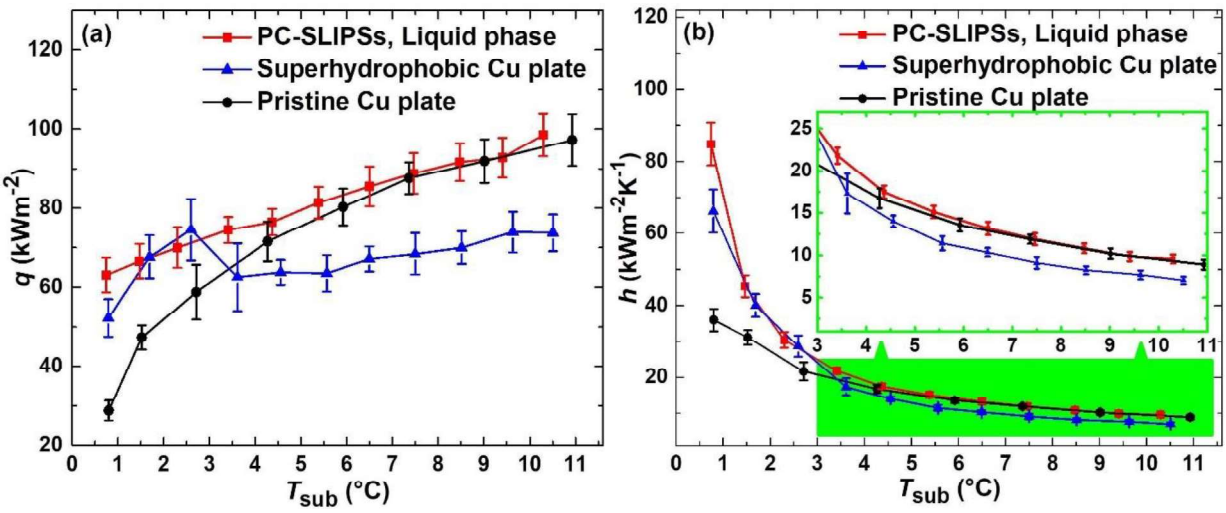

Fig. 6. (a) Heat flux q (kWm^{-2}), and (b) heat transfer coefficient h ($kWm^{-2}K^{-1}$) versus sub-cooling temperature T_{sub} (°C) on the pristine Cu (copper) plate, superhydrophobic Cu plate and liquid phase of the PC-SLIPSs

In all cases (pristine copper plate, superhydrophobic copper plate and PC-SLIPSs) the heat flux q increases with T_{sub} as expected. For the moderate and low sub-cooling temperatures T_{sub} <

5 °C, the heat flux q (Fig. 6a) is higher for PC-SLIPSs in the liquid phase when compared to the pristine copper plate and superhydrophobic copper plate. For higher sub-cooling conditions T_{sub} > 5 °C, q is relatively comparable on both surfaces (pristine copper plate and PC-SLIPSs), while it is lower on superhydrophobic copper plate. Indeed, at high T_{sub}, higher condensate rate or condensate growth ensues, compared to the discrete droplet shedding or coalescence-induced droplet shedding of sub-millimeter droplets at low T_{sub} [42], and flooding may occur [43]. When looking at PC-SLIPSs in the liquid phase, the heat transfer coefficient h in Fig. 6b is averagely 136.8% higher than that of the pristine copper surface at equivalent low sub-cooling temperature of around 0.8 °C and nearly 50% higher at T_{sub} = 1.5 °C as reported earlier in Fig. 5. As the sub-cooling temperature is increased (T_{sub} > 4 °C), the heat transfer coefficients h for the pristine copper and PC-SLIPSs in the liquid phase approach each other [44]. Indeed, at high range of T_{sub}, the higher generation rate of the condensate [42][43] compared with its prompt shedding may be ensued, and under such conditions, the overflow of liquid adopting the channel-like pattern in filmwise mode may become faster on the pristine copper plate than that of PC-SLIPSs and superhydrophobic copper plate providing the dropwise mode. In particular, on PC-SLIPSs, the transient degradation of paraffin wax might have been large until reaching the high sub-cooling temperatures (we did experiments on surfaces continuously starting from low sub-cooling to high sub-cooling conditions) due to which the condensation performance is compromised.

Based on the effective droplet dynamics and heat transfer performance solely in the liquid phase, the transient durability analysis of the PC-SLIPSs has been conducted under saturated steam condensation (steam temperature of 70 °C). The droplet dynamics has been carefully observed during the experiments. It has been found that PC-SLIPSs can continuously work for

about 8±1 hours, depicting the effective durability in operation. Beyond that duration, the droplet dynamics are highly compromised together with strong droplet pinning, as demonstrated in Fig. 7a. After the durability experiments, a 5 µL water droplet encounters immobility even at the sliding angle of 60° (Fig. 7b) and surface temperature of 66 °C in opposed to very small sliding angle before condensation (Table 1). Further, upon looking into the surface morphology (solid phase has been observed at ambient temperature under confocal laser scanning microscopy) as demonstrated in Fig. 7c, the considerable loss of paraffin wax has been found, and randomly dispersed paraffin wax is available which is in great contrast to what has been observed before condensation (Fig. 3a). We attribute the surface instability of PC-SLIPSs to the loss of paraffin wax induced by the physical shearing and viscous dissipation; because chemically, paraffin waxes are inert and immiscible with water, thus prohibiting the cloaking-induced [29][33] surface instability.

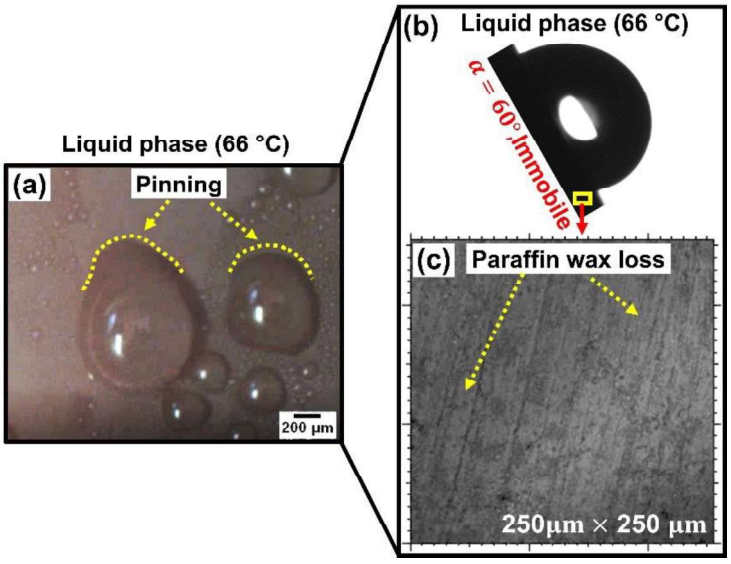

Fig. 7. Transient durability of PC-SLIPSs in liquid phase during water vapor condensation, (a) droplet pinning after continued for 8±1 hours of operation, (b) advancing and receding angles (c) confocal laser scanning microscopic image depicting paraffin loss after durability analysis

3.2. Dropwise condensation modeling and heat transfer mechanism

Discrete-droplet shedding and sweeping events entailing the droplets with small r_{cd} in the submillimeter range and rapid t_s in the liquid phase of PC-SLIPSs are highly favorable for steam condensation applications as it minimizes the effective droplet-surface interactions while maximizing the shedding dynamics, in turn beneficial for heat transfer. To this end, the droplet population on the condensing surfaces is a key parameter closely related to the heat transfer performance and utilized for the estimation of steady state heat transfer [23][24][25]. The droplet population can be predicted via the experimental droplet number density $N_e(r)$ (drops/mm^3) which is an experimental estimation of total number of droplets N_d distributed (either randomly or regularly) in a certain range of droplet radii r over an investigated area A, as given follows:

$$N_e(r) = \frac{(N_d/A)}{r} \tag{1}$$

It should be noted that $N_e(r)$ is solely based on the steady state droplet population, which in turn shall be the function of the wettability and structure of the surface, the properties of the condensing liquid and the environment as well as the temperature and saturation conditions. In order to extract N_d from our experimental observations, we make use of ImageJ software following a stepwise image processing, as depicted in Fig. 8. The raw image containing the condensed droplets is imported into ImageJ and the scale is set (Fig. 8a). Then, big sized droplets are manually encircled and cut to enhance the contrast between the droplets and the background, as shown in Fig. 8b. Afterwards, a threshold is applied to adjust the color (black and white) of the image, as shown in Fig. 8c, which results in the clear visualization of small-sized droplets. Finally, the numbers of droplets are analyzed by applying "Analyze Particles" in which "droplet outlines" are fitted to the droplets and highlighted, as shown in Fig. 8d. The analysis then returns the surface area of the fitted circle A_d. Data is then transferred into an Excel file, the droplet

radius r is estimated from A_d as $r = \sqrt{A_d/\pi}$. Then droplets are categorized into certain radii ranges and then those within the same range are counted. We note here that r is the droplet radius, i.e., sphere radius, which differs from the droplet base radius. Based on the limitations of droplet cut at the edges and the surrounding of smaller droplets by the larger droplets, the total number of droplet count has been presented within ±18.

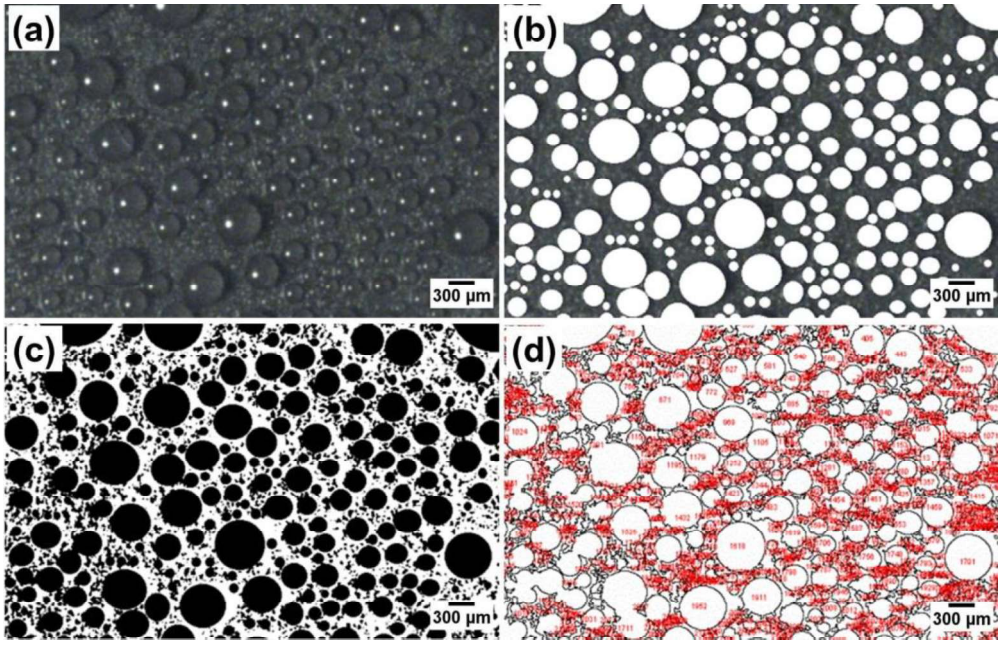

Fig. 8. Method to measure the droplet numbers and data extraction for droplet number density from ImageJ, (a) the raw image (cropped from the original image), (b) big sized droplets cut, (c) color (black and white) adjustment via threshold application for retrieving small-sized droplets, and (d) extraction of droplet outlines with droplet areas.

In addition, theoretical predictions for droplet number density $N_t(r)$ (drops/mm^3) have also been conducted by employing Rose model developed for hydrophobic surfaces, which can be applied to the SLIPSs with similar advancing angle $\theta_{adv} \sim 120°$ as in the work of Weisensee [24] and Maeda et al., [25]. The Rose model is given as follows [45]:

$$N_t(r) = \left(\frac{1}{3\pi r^2 r_{max}}\right)\left(\frac{r}{r_{max}}\right)^{\frac{-2}{3}} \quad (2)$$

where r is the droplet radius, and r_{max} is the maximum droplet radius (the droplet shedding radius r_{cd}) as given in Eq. S13 [23] in Supplementary Material. However, it is noted that $r_{max,Rose}$ is independent of the surface wetting features such as the advancing angles, receding angles and contact angle hysteresis. Nonetheless, on smart and/or functionalized surfaces r_{max} is actually highly dependent on the surface features such as wettability and surface structure as it was conveyed above, see Table 1. To accommodate our theoretical estimation of the droplet number density and that of the theoretical heat flux to the different surface wetting features, we make use of r_{max} proposed by Kim and Kim as $r_{max,Kim}$, which is given in Eq. S14 [23] in Supplementary Material. Therefore, Rose model (Eq. 2) taking the surface properties into account via $r_{max,Kim}$ is modified as follows:

$$N_t(r) = \left(\frac{1}{3\pi r^2 \sqrt{\frac{6sin\theta_m\sigma_w(cos\theta_{rec}-cos\theta_{adv})}{\pi\rho_w g(2-3cos\theta_m+cos^3\theta_m)}}}\right)\left(\frac{r}{\sqrt{\frac{6sin\theta_m\sigma_w(cos\theta_{rec}-cos\theta_{adv})}{\pi\rho_w g(2-3cos\theta_m+cos^3\theta_m)}}}\right)^{-\frac{2}{3}} \quad (3)$$

where θ_m (°) (Eq. S15 in Supplementary Material) is the mean of advancing angle θ_{adv} (°) and receding angle θ_{rec} (°) [24].

The experimental droplet number density $N_e(r)$ for PC-SLIPSs in the liquid phase is plotted as the function of droplet radius r in Fig. 9. The droplet number density $N_e(r)$ presented in Fig. 9 takes the form of $N_e(r) = ar^{-b}$,where a and b are constants with values of 1.14×10^6 and 2.65, respectively. The regression model defining the $N_e(r)$ for liquid phase of the PC-SLIPSs finds a closer match to the model defined by Ho et al., with a and b of 3.76×10^6 and 2.44 [26], while deviates from those earlier reported on lubricant infused surfaces by Weisensee et al., [24] and Maeda et al., [25], which are in the order of 10^7 and between 3.2 and 4.0. Quantitative differences between the experimental droplet number density reported in this work and those

reported in Weisensee et al., [24] and Maeda et al., [25] can be attributed to the different sub-cooling temperatures, different condensing condition (steam condensation versus condensation in ambient atmosphere in the presence of non-condensable gases) and to the impossibility to implement optical microscopy during steam condensation opposed to Ref. [24] and Ref. [25]. We note here that the population of droplets with radius below 80 μm is rather large. The experimental droplet density can then be estimated as $N_e(r) = 1.14\times10^6 r^{-2.65}$, which shows a good agreement with the theoretical droplet number density proposed by Rose $N_t(r)$ (Rose model, Eq. 2), as depicted in Fig. 9.

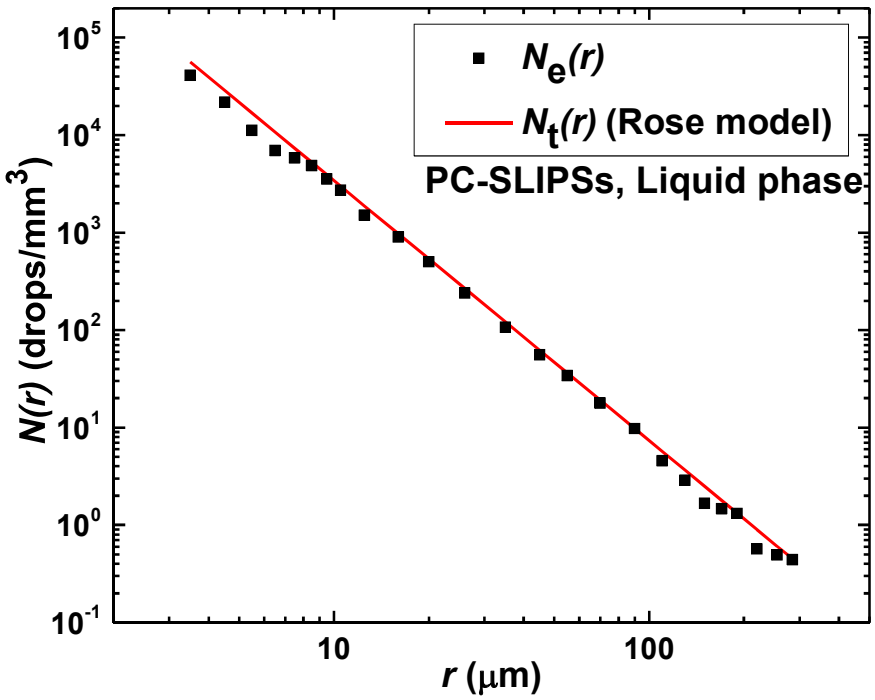

Fig. 9. Experimental $N_e(r)$ and theoretical $N_t(r)$ droplet number density (drops/mm^3) versus droplet radius r (μm).

By making use of the droplet number density $N_e(r)$, the theoretical heat flux q_t (kWm^{-2}) on a condensing surface can be determined, which is given below as [23][24]:

$$q_t = \int_{r_{min}}^{r_{max}} q_d(r).N_e(r)dr \tag{4}$$

where, q_d is the heat transfer rate through a single droplet that is in turn a function of the droplet radius r. Therefore, $N_e(r)$ is a representative parameter for dropwise condensation heat transfer. r_{max} and r_{min} are the droplet radii indicating the maximum droplet size and minimum droplet size that are related to the droplet shedding and the radius for nucleation, respectively. As stated above, r_{max} can be estimated via the Kim and Kim model (Eq. S14 in Supplementary Material), and r_{min} can be estimated through Kelvin equation [46] as given in Eq. S16 in Supplementary Material. However, it should be noted that r_{min} as predicted theoretically could not be determined experimentally, which is due to the limitation of implementing optical microscopy observations through the environmental chamber. Other advanced techniques such as environmental scanning electron microscopy (ESEM) may provide enough spatial resolution to resolve the droplet nucleation phase at nanoscopic scale, although the exact experimental conditions of this work would be possible. ESEM fails to work at high operational temperature equivalent to the liquid phase PC-SLIPSs which is 60 °C and it is also not suitable for inducing the sub-cooling conditions [47].

In dropwise condensation, r_{max} and r_{min} are delimited by an effective radius r_e defined as $r_e = \frac{1}{\sqrt{4N_s}}$ where N_s is the number of nucleation sites per unit area of the condensing surface. Typically N_s can lie in the range of 10^3~10^7 (drops/mm^2) [48][49]. The effective radius r_e additionally defines the regions at which droplet growth via direct condensation occurs for $r < r_e$ or via both direct condensation and coalescence for $r > r_e$. Then, the theoretical heat transfer model can be divided in two parts comprising the droplet number density $n_e(r)$ with droplet radii smaller than r_e and the droplet number density $N_e(r)$ with droplet radii larger than r_e, as given below [50]:

$$q_{\mathrm{t}} = \int_{r_{\min}}^{r_{\mathrm{e}}} q_{\mathrm{d}}(r) n_{\mathrm{e}}(r) dr + \int_{r_{\mathrm{e}}}^{r_{\max}} q_{\mathrm{d}}(r) N_{\mathrm{e}}(r) dr \tag{5}$$

where $n_e(r)$ has been addressed by Eq. S17 [26][51] as given in the Supplementary Material.

Next, the heat transfer through a single droplet q_d is formulated with the help of a thermal resistance approach as follows [23][24]:

$$q_{\mathrm{d}} = \frac{T_{sub/t}}{R_{\mathrm{t}}} \tag{6}$$

where $T_{sub/t}$ is the theoretical sub-cooling temperature (Eq. S19 in Supplementary Material) and R_t is the total thermal resistance. The encountered thermal resistances across the droplet and the surface are further elaborated in Fig. S4 and Section 3 in Supplementary Material.

Thus, by implementing all the thermal resistances in Eq. 7, the heat transfer rate q_d through a single droplet on SLIPSs is estimated as follows:

$$q_{\mathrm{d}} = \frac{(\pi r^2) T_{sub/t}}{\left(\frac{1}{2h_{\mathrm{i}}(1-cos\theta_{adv})}\right) + \left(\frac{r\theta_{\mathrm{adv}}}{4k_{\mathrm{w}} sin\theta_{\mathrm{adv}}}\right)} \tag{7}$$

By employing the developed model, the theoretical heat transfer rate q_d (Eq. 7) through a single droplet of varying radii at various sub-cooling temperatures T_{sub} for liquid phase of the PC-SLIPSs is shown in Fig. 10a, while the overall theoretical heat flux q_t (Eq. 5) as the function of sub-cooling temperature T_{sub} is further represented in Fig.10b.

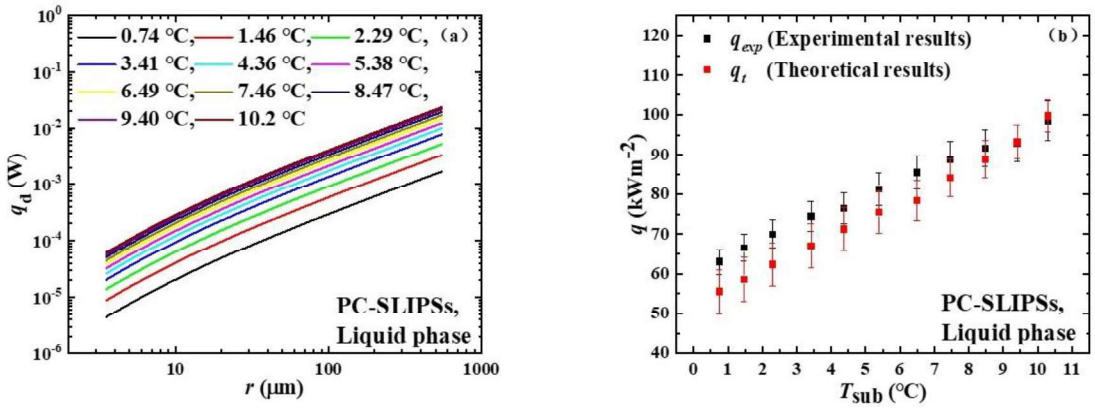

Fig. 10. (a) Theoretical heat transfer rate q_d via a single droplet for the PC-SLIPSs in liquid phase versus droplet radius r (μm) and sub-cooling temperature T_{sub} (°C). (b) Overall theoretical heat flux q_t (kWm^{-2}) and experimental heat flux q_{exp} (kWm^{-2}) versus sub-cooling temperature T_{sub} (°C)

It is thus clear that q_d is affected by the different droplet radius ranges. At a constant sub-cooling temperature, q_d increases as the function of droplet radii which is enabled by the direct increase in the droplet area for heat transfer (despites the greater thermal resistance imposed) that correlates with r. Further, with increasing the sub-cooling temperature, the heat transfer through single droplets also increases. Both effects can be inferred by looking at Eq. 7 where both r and T_{sub} contribute directly proportional to the heat transfer rate q_d through single droplet. When comparing the theoretical and experimental heat fluxes, i.e., q_t vs q_{exp}, mild differences are noted, as shown in Fig. 10b. In the classical model by Le Fevre and Rose [45], $N_e(r)$ is only a function of r and has no direct correlation with the sub-cooling temperature, which apparently does not provide a satisfactory description of $N_e(r)$ under the current sub-cooling temperature span. Even at the same sub-cooling temperature, the condensation images at different time instants usually show different droplet distribution, which leads to a fluctuation of the theoretical heat flux. Therefore, an average theoretical heat flux is shown in Fig. 10b. It should be noted that in the

calculation of theoretical heat flux q_t by using Eq. 5, the droplet number density $N_e(r)$ (Eq. 1) is extracted directly from the visualization images at various sub-cooling temperatures, which is described in detail in Section 4 in Supplementary Material. Shown in Fig. S5 and Table S1 are the examples of the results of $N_e(r)$ at three typical sub-coolings. At lower sub-cooling temperature, the quantity of small-sized droplet is large and that of large-sized droplet is small, which might leads to a larger uncertainty in image process, and it is reverse at higher sub-cooling temperature.

4. Conclusions

PC-SLIPSs have been prepared by infusing the paraffin-wax xylene solution in the superhydrophobic nano-porous scaffold of the oxidized copper plates. The interaction of PC-SLIPSs with water droplets can be promisingly tuned via phase-dependent wetting characteristics of paraffin wax. The water vapor condensation has been comprehensively studied on PC-SLIPSs in the custom-built vacuum-assisted condensation rig. It has been found that each phase of PC-SLIPSs can help induce dropwise condensation of saturated water vapors, however the droplet dynamics is different due to the extent of droplet adhesion, i.e., low adhesion in solid phase, high adhesion in mush phase and virtually negligible adhesion in liquid phase. Based on the discrete-droplet shedding-sweeping mechanism in the liquid phase, high heat transfer performance (by 136.8% higher h) compared to filmwise condensation on the pristine copper surface is therefore reported. In liquid phase, PC-SLIPSs can effectively operate during rigorous steam condensation for about 8±1 hours by maintaining the efficient droplet dynamics, and afterwards, the droplet dynamics has been drastically affected which is ascribed to the loss of paraffin wax by the physical shearing. In addition, theoretical modeling of dropwise condensation in liquid phase of PC-SLIPSs confirms the greater heat transfer performance by

smaller droplet radii. A good match has been found between the experimental and theoretical parameters. Guided by the results, the liquid phase of PC-SLIPSs conforming to the slippery state is declared to be only promisingly effective for the condensation heat transfer in comparison with solid and mush phases. As PCMs are available in the wide range of melting temperatures, PC-SLIPSs can be tailored for the desired (low) operational temperature maintaining only liquid phase particularly in condensation either for heat transfer or water harvesting applications. Altogether, this research carefully implies that only dropwise condensation mode is not the key to enhance the heat transfer performance, yet the fast droplet dynamics even in dropwise mode should be of prime consideration which is mainly influenced by the surface topography.

Acknowledgment

This research is supported by the National Natural Science Foundation of China under the Contract No. 51976117. A few characterizations are conducted in the AEMD of Shanghai Jiao Tong University. D.O. additionally acknowledges the support from the International Institute for Carbon-Neutral Energy Research (WPI-I2CNER), sponsored by the Japanese Ministry of Education, Culture, Sports, Science, and Technology; and The Royal Society Research Grant 2020 Round 2 with Reference RGS/R2/202041.

References

[1] R. Wen, X. Ma., Advances in dropwise condensation: dancing droplets, 21st century surface science-a handbook, IntechOpen (2020) 92689.

[2] N. Pionnier, J. Vera, E. Contraires, S. Benayoun, Rémi Berger, S. Valette, The effect of the orientation and the height of periodic sub-micrometric texturing on dropwise condensation, Journal of Colloid and Interface Science 526 (2018) 184-193.

[3] Z. Deng, C. Zhang, C. Shen, J. Cao, Y. Chen, Self-propelled dropwise condensation on a gradient surface, International Journal of Heat and Mass Transfer 114 (2017) 419429.

[4] R. Xiao, N. Miljkovic, R. Enright, E. N. Wang, Immersion condensation on oil-infused heterogeneous surfaces for enhanced heat transfer, Scientific Reports 3 (2013) 1988.

[5] H. M. Ali, Condensation heat transfer on geometrically enhanced horizontal tube: a review, Heat exchangers-advanced features and applications, IntechOpen (2017) 65896.

[6] B. E. Fil, G. Kini, S. Garimella, A review of dropwise condensation: Theory, modeling, experiments, and applications, International Journal of Heat and Mass Transfer 160 (2020) 120172.

[7] J. Ma, S. Sett, H. Cha, X. Yan, N. Miljkovic, Recent developments, challenges, and pathways to stable dropwise condensation: A perspective, Applied Physics Letters 116 (2020) 260501.

[8] Rose JW. Dropwise condensation theory and experiment: A review. Proceedings of the Institution of Mechanical Engineers Part A: Journal of Power and Energy 216 (2) (2002) 115-128.

[9] J.-D. Smith, R. Dhiman, S. Anand, E. R.-Garduno, R. E. Cohen, G. H. McKinleya, K. K. Varanasi, Droplet mobility on lubricant-impregnated surfaces, Soft Matter 9(6) (2013)1772-1780.

[10] D. Daniel, J. V. I. Timonen, R. Li, S. J. Velling, J. Aizenberg, Oleoplaning droplets on lubricated surfaces, Nature Physics 13(10) (2017)1020-1025.

[11] T. S. Wong, S. H. Kang, S. K. Y. Tang, E. J. Smythe, B. D. Hatton, A. Grinthal, J. Aizenberg, Bioinspired self-repairing slippery surfaces with pressure-stable omniphobicity, Nature 477 (2011) 443-447.

[12] S. Peppou-Chapman, J. K. Hong, A. Waterhouse, and C. Neto, Life and death of liquid-infused surfaces: a review on the choice, analysis and fate of the infused liquid layer, Chemical Society Reviews 49 (11) (2020) 3688-3715.

[13] G. K. Sirohia, X. Dai, Designing air-independent slippery rough surfaces for condensation, International Journal of Heat and Mass Transfer 140 (2019) 777-785.

[14] S. Anand, A. T. Paxson, R. Dhiman, J. D. Smith, K. K. Varanasi, Enhanced condensation on lubricant-impregnated nanotextured surfaces, ACS Nano 6(11) (2012) 10122-10129.

[15] P. Baumli, M. D'Acunzi, K. I. Hegner, A. Naga, W. S. Y. Wong, H. J. Butt, D. Vollmer, The challenge of lubricant-replenishment on lubricant-impregnated surfaces, Advances in Colloid and Interface Science 287 (2021) 102329.

[16] S. Adera, J. Alvarenga, A. V. Shneidman, C. T. Zhang, A. Davitt, J. Aizenberg, Depletion of lubricant from nanostructured oil-infused surfaces by pendant condensate droplets, ACS Nano 14(7) (2020) 8024-8035.

[17] X. Chen, G. Wen, Z. Guo, What are the design principles, from the choice of lubricants and structures to the preparation method, for a stable slippery lubricant-infused porous surface?, Material Horizon 2020 7 (2020) 1697-1726.

[18] H. Tsuchiya, M. Tenjimbayashi, T. Moriya, R. Yoshikawa, K. Sasaki, R. Togasawa, T. Yamazaki, K. Manabe, S. Shiratori, Liquid-infused smooth surface for improved condensation heat transfer, Langmuir 33(36) (2017) 8950–8960.

[19] J. Sablowski, S. Unz, M. Beckmann, Dropwise condensation on advanced functional surfaces–theory and experimental set-up, Chemical Engineering & Technology 40 (11) (2017) 1966.

[20] L. Guo and G. H. Tang, Dropwise condensation on bioinspired hydrophilic-slippery surface, RSC Advances 8 (69) (2018) 39341-39351.

[21] J.W. Rose, Dropwise condensation theory, International Journal of Heat and Mass Transfer 24 (1981) 191-194.

[22] J.W. Rose, Dropwise condensation theory and experiment: a review, Proceedings of the Institution of Mechanical Engineers Part A: Journal of Power & Energy 216 (2001) 115-128.

[23] S. Kim, K.J. Kim, Dropwise condensation modeling suitable for superhydrophobic surfaces, Journal of Heat Transfer 133 (2011) 081502.

[24] P. B. Weisensee, Y. Wang, Q. Hongliang, D. Schultz, W. P. King, N. Miljkovic, Condensate droplet size distribution on lubricant-infused surfaces, International Journal of Heat and Mass Transfer 109 (2017) 187-199.

[25] Y. Maeda, F. Y. Lv, P. Zhang, Y. Takata, and D. Orejon, Condensate droplet size distribution and heat transfer on hierarchical slippery lubricant infused porous surfaces, Applied Thermal Engineering 176 (2020) 115386.

[26] J.Y. Ho, K.F. Rabbi, S. Sett, T.N. Wong, N. Miljkovic, Dropwise condensation of low surface tension fluids on lubricant-infused surfaces: Droplet size distribution and heat transfer, International Journal of Heat and Mass Transfer 172 (2021) 121149.

[27] R. Gulfam, P. Zhang, Z. Meng, Advanced thermal systems driven by paraffin-based phase change materials–A review, Applied Energy 238 (2019) 582-611.

[28] R. Gulfam, P. Zhang, Power generation and longevity improvement of renewable energy systems via slippery surfaces-A review, Renewable Energy 143 (2019) 922-938.

[29] R. Gulfam, D. Orejon, C. H. Choi, P. Zhang, Phase-change slippery liquid-infused porous surfaces with thermo-responsive wetting and shedding states, ACS Applied Materials & Interfaces 12 (30) (2020) 34306-34316.

[30] X. Yao, J. Ju, S. Yang, J. Wang, L. Jiang, Temperature-driven switching of water adhesion on organogel surface, Advanced Materials 26 (12) (2014) 1895.

[31] Z. Wang, Q. Xu, L. Wang, L. Heng, L. Jiang, Temperature-induced switchable interfacial interactions on slippery surfaces for controllable liquid manipulation, Journal of Materials Chemistry A **7** (31) (2019) 18510.

[32] C. Chen, L. Zhou, L. A. Shi, S. Zhu, Z. Huang, C. Xue, J. Li, Y. Hu, D. Wu, J. Chu, Ultralow-voltage-driven smart control of diverse drop's anisotropic sliding by in situ switching joule heat on paraffin-infused microgrooved slippery surface, ACS Applied Materials and Interfaces 12(1) (2020) 1895-1904.

[33] K. Manabe, T. Matsubayashi, M. Tenjimbayashi, T. Moriya, Y. Tsuge, K. H. Kyung, S. Shiratori, Controllable broadband optical transparency and wettability switching of temperature-activated solid/liquid-infused nanofibrous membranes, ACS Nano 10 (10) (2016) 9387.

[34] F. Wang, S. Luo, S. Xiao, W. Zhang, Y. Zhuo, J. He, Z. Zhang, Enabling phase transition of infused lubricant in porous structure for exceptional oil/water separation, Journal of Hazardous Materials 390 (2020) 122176.

[35] F. Wang, W. Ding, J. He, Z. Zhang, Phase transition enabled durable anti-icing surfaces and its DIY design, Chemical Engineering Journal 360 (2019) 243-249.

[36] R. Chatterjee, D. Beysens, S. Anand, Delaying ice and frost formation using phase-switching liquids, Advanced Materials 31(17) (2019) 1807812.

[37] D. Wu, L. Ma, F. Zhang, H. Qian, B. Minhas, Y. Yang, X. Han, D. Zhang, Durable deicing lubricant-infused surface with photothermally switchable hydrophobic/slippery property, Materials & Design 185 (2020) 108236.

[38] H.-Q, Jin, S. Wang, Experimental study of refrigerant (R-134a) condensation heat transfer and retention behavior on paraffin-coated vertical plates and fin structures, Journal of Heat Transfer 142(8) (2020) 081601.

[39] P. Zhang, F. Y. Lv, A. Askounis, D. Orejon, B. Shen, Role of impregnated lubricant in enhancing thermosyphon performance, International Journal of Heat and Mass Transfer 109 (2017) 1229-1238.

[40] C. G. J. Prakash, R. Prasanth, Recent trends in fabrication of nepenthes inspired SLIPSs: Design strategies for self-healing efficient anti-icing surfaces, Surfaces and Interfaces 21 (2020) 100678.

[41] R. McCerery, J. Woodward, G. McHale, K. Winter, S. Armstrong, and B. V. Orme, Slippery liquid-infused porous surfaces: The effect of oil on the water repellence of hydrophobic and superhydrophobic soils, European Journal of Soil Science 72 (2) (2020) 963-978.

[42] J. Cheng, A. Vandadi, C.-L. Chen, Condensation heat transfer on two-tier superhydrophobic surfaces, Applied Physics Letters 101 (2012) 131909.

[43] R. Wen, Q. Li, J. Wu, G. Wu, W. Wang, Y. Chen, X. Ma, D. Zhao, R. Yang, Hydrophobic copper nanowires for enhancing condensation heat transfer, Nano Energy 33 (2017) 177183.

[44] T. Y. Zhang, L. W. Mou, J. Y. Zhang, L. W. Fan, J. Q. Li, A visualized study of enhanced steam condensation heat transfer on a honeycomb-like microporous superhydrophobic surface in the presence of a non-condensable gas, International Journal of Heat and Mass Transfer 150 (2020) 119352.

[45] E.J. Le Fevre, J.W. Rose, A theory of heat transfer by dropwise condensation, Third International Heat Transfer Conference (1966).

[46] V.P. Carey, Liquid-vapor phase-change phenomena: An introduction to the thermophysics of vaporization and condensation processes in heat transfer equipment, Taylor and Francis, New York, 2008.

[47] D. Orejon, O. Shardt, P. R. Waghmare, N. S. K. Gunda, Y. Takata, S. K. Mitra, Droplet migration on chemically patterned micropillared surfaces, RSC Advances 6 (2016) 36698-36704.

[48] H. R. T. Bahrami, H. Saffari, Mathematical modeling and numerical simulation of dropwise condensation on an inclined circular tube, Journal of Aerospace Technology & Management 9 (2017) 476-488.

[49] S. Vemuri, K.J. Kim, An experimental and theoretical study on the concept of dropwise condensation, International Journal of Heat and Mass Transfer 49 (3-4) (2006) 649-657.

[50] H. Tanaka, A theoretical study of dropwise condensation, Journal of Heat Transfer 97 (1975) 72-78.

[51] J. Wang, Z. Ma, G. Li, B. Sundén, J. Yan, Improved modeling of heat transfer in dropwise condensation, International Journal of Heat and Mass Transfer 155 (2020) 119719.